

Multi-color blackbody emission in GRB 081221

Shu-Jin Hou^{1,2,3,4}, Bin-Bin Zhang^{5,6}, Yan-Zhi Meng², Xue-Feng Wu², En-Wei Liang³,
Hou-Jun Lü³, Tong Liu⁷, Yun-Feng Liang², Lin Lin⁸, Rui-jing Lu³, Jin-Shu Huang^{1,4}, and
Bing Zhang⁹

ABSTRACT

The radiation mechanism of the prompt emission of gamma-ray bursts (GRBs) remains an open question. Although their spectra are usually well fitted with the empirical Band function, which is widely believed to be fully non-thermal and interpreted as an optically thin synchrotron emission, accumulating evidence shows that a thermal component actually exists. In this paper, a multi-color blackbody (mBB) model is proposed for the time-integrated spectrum of GRB 081221 by assuming a power-law distribution of the thermal luminosities with temperature, which manifests photospheric emissions from a different radius and/or angle. The effects of the minimum temperature kT_{\min} , the maximum temperature kT_{\max} and the power law index m of the luminosity distribution of an mBB are discussed. The fitting to the time-integrated spectrum during the bright phase (from 20s to 30s since the trigger) of GRB 081221 by the mBB

¹College of Physics and Electronic Engineering, Nanyang Normal University, Nanyang, Henan, 473061, China

²Purple Mountain Observatory, Chinese Academy of Sciences, Nanjing 210008, China; xfwu@pmo.ac.cn

³Department of Physics and GXU-NAOC Center for Astrophysics and Space Sciences, Guangxi University, Nanning 530004, China; lew@gxu.edu.cn

⁴Key Laboratory for the Structure and Evolution of Celestial Objects, Chinese Academy of Sciences, Kunming 650011; China

⁵School of Astronomy and Space Science, Nanjing University, Nanjing 210093, China; bbzhang@nju.edu.cn

⁶Key Laboratory of Modern Astronomy and Astrophysics (Nanjing University), Ministry of Education, China

⁷Department of Astronomy, Xiamen University, Xiamen, Fujian 361005, China

⁸Department of Astronomy, Beijing Normal University, Beijing 100875, China

⁹Department of Physics and Astronomy, University of Nevada, Las Vegas, NV 89154; zhang@physics.unlv.edu

model yields $kT_{\min} = 4.4 \pm 0.3$ keV, $kT_{\max} = 57.0^{+1.6}_{-1.4}$ keV, and $m = -0.46^{+0.05}_{-0.06}$. When the time bin is small enough, the time-resolved spectra of GRB 081221 are well fitted with a series of single-temperature blackbodies. Our results imply the prompt emission of GRB 081221 is dominated by the photosphere emission and its time-integrated spectrum is a superposition of pure blackbody components at different times, indicating that some empirical Band spectra may be interpreted as mBB if the temperature is widely distributed.

Subject headings: gamma-rays burst: individual - radiation mechanisms: thermal

1. Introduction

The prompt emission is the earliest detected signal of gamma-ray bursts (GRBs). However, its physical origin, closely related to the ejecta composition, energy dissipation, particle acceleration, and especially the radiation mechanism (e.g., Zhang 2011; Gao & Zhang 2015; Bégué & Pe’er 2015; Pe’er et al. 2015), is still a very controversial topic after more than forty years.

Thermal emission in the relativistic fireball model is a natural explanation for the prompt emission (Goodman et al. 1986), since the optical depth at the base of the outflow is much larger than unity and it well explains the observed small dispersion of the sub-MeV peak and high prompt emission efficiency (Mészáros & Rees 2000, Rees & Mészáros 2005). But in Compton GRO/BATSE era, the observed GRB spectra are well fitted by an empirical smoothly-jointed broken power law, which is the so-called “Band” function (Band et al. 1993). Compared to a blackbody function, this spectrum has a much wider peak, and it is much softer at low energies. For a long time, such a spectral shape is widely believed to be produced by optically thin synchrotron processes. Band function is then used to phenomenologically capture this shape. However, previous studies using both Compton/BASTE and Fermi/GBM data have shown that some observed low-energy spectra are found to be harder than that predicted by the synchrotron model in a substantial fraction of GRBs (Preece et al. 1998; Kaneko et al. 2006; Gruber et al. 2014) and the spectral width of some GRBs is found to be very narrow (Axelsson & Borgonovo 2015; Yu et al. 2015). These facts suggest that a quasi-thermal component should exist, which has been observationally confirmed lately. The early examples include tens of BATSE GRBs (Ryde 2005, Ryde & Pe’er 2009). Thanks to Fermi’s unprecedented spectral energy coverage (GBM: 8 keV to 40 MeV, Meegan et al. 2009; LAT: 20 MeV to >300 GeV, Atwood et al. 2009), we now have several such examples among the Fermi detected GRBs, such as GRB 090902B (Abdo et al. 2009; Ryde et al. 2010; Zhang et al. 2011), GRB 100724B (Guiriec et al. 2011), GRB 110721A (Axelsson et

al. 2012), GRB 100507 (Ghirlanda et al. 2013), GRB 120323A (Guiriec et al. 2013) and GRB 101219B (Larsson et al. 2015). The thermal emission is also claimed to exist in some early X-ray flares of GRBs (Peng et al. 2014).

GRB 081221 was jointly detected by Fermi/GBM (Wilson-Hodge 2008), the Burst Alert Telescope (BAT) on board Swift (Hoversten et al. 2008; Cummings et al. 2008), and Konus/Wind (Golenetskii et al. 2008). The X-ray telescope on board Swift found the early-time X-ray afterglow (Stroh & Hoversten 2008). The faint optical and radio afterglows were also detected (Kuin & Hoversten 2008; Chandra & Frail 2008). Multi-wavelength observations of this burst provide the opportunity to explore the physical origin of the GRB. Especially, the spectral properties of its prompt emission are similar to those of GRB 090902B (Pe’er & Ryde 2011; Ryde et al. 2010; Mizuta et al. 2011; Toma et al. 2011), showing a prominent thermal component. In this work, we perform both the time-integrated and time-resolved spectral analysis of the prompt emission of GRB 081221, to achieve the characteristic of the thermal component.

In §2, we give a short description of our model. The time-integrated and time-resolved spectral analysis are presented in §3. Conclusions are drawn in §4 with some discussion.

2. Multi-color blackbody spectra

In the standard fireball model of GRBs, the photons produced in the outflow are thermalized, and they can escape near the photospheric radius r_{ph} , where the optical depth is equal to 1. In a relativistic, spherically symmetric wind, the photospheric radius is found to be a function of the angle to the line of sight (Abramowicz et al. 1991; Pe’er 2008; Meng et al. 2018), $r_{\text{ph}} = r_{\text{ph}}(\theta)$. This means that the observed spectrum is a superposition of a series of blackbodies of different temperature, arising from different angles to the line of sight. Furthermore, considering that photons have a finite probability of being scattered at any point in space where electrons exist, Pe’er (2008) introduced the probability density distributions for the last scattering photon positions, $P(r, \theta)$. Then, the observed spectrum is contributed by photons from the entire emitting volume, so it is certainly a multi-color blackbody (mBB). Several works have tried to explain the Band function as originated from the mBB by taking into account more realistic outflow (Pe’er & Ryde 2011; Beloborodov et al. 2011; Lundman et al. 2013; Ito et al. 2013; Deng & Zhang 2014).

The photon spectrum of a cosmological GRB with a single temperature kT , with luminosity L_{BB} defined in the host galaxy frame and the luminosity distance D_L can be given

as

$$N(E) = \frac{15}{4\pi^5} \frac{L_{\text{BB}}}{D_L^2 (kT)^4} \frac{E^2}{e^{E/kT} - 1}. \quad (1)$$

Technically, the formula for the photon spectrum of a blackbody usually used in the spectral fitting is

$$N(E) = \frac{8.0525K}{(e^{E/kT} - 1)} \left(\frac{kT}{\text{keV}} \right)^{-4} \left(\frac{E}{\text{keV}} \right)^2, \quad (2)$$

where $N(E)$ is in units of $\text{ph cm}^{-2} \text{ s}^{-1} \text{ keV}^{-1}$, and kT and E are measured in the observer's frame. $K = L_{39}/D_{L,10\text{kpc}}^2$ is defined by the blackbody luminosity L in units of $10^{39} \text{ erg s}^{-1}$ in the GRB host galaxy frame and the luminosity distance D_L in units of 10 kpc.

For mBB, different from the **probability distribution** of the mBB temperature in Ryde et al. (2010), we assume that the dependence of the luminosity distribution on the temperature has a power-law form,

$$\frac{dL}{dT} = \frac{m+1}{\left[\left(\frac{T_{\text{max}}}{T_{\text{min}}} \right)^{m+1} - 1 \right]} \frac{L_{\text{mBB}}}{T_{\text{min}}} \left(\frac{T}{T_{\text{min}}} \right)^m, \quad (3)$$

where m is the power-law index of the distribution, and the temperature ranges from the minimum T_{min} to the maximum T_{max} , and $L_{\text{mBB}} = \int_{T_{\text{min}}}^{T_{\text{max}}} dL$ is the total luminosity of the mBB. Compared with the previous treatment, Eq. (3) is more directly related to the physics of the GRB fireball, since it may imply the dependence of the luminosity (rather than temperature) in different radius or angle. Combining the above equations, the photon spectrum of the mBB can be formulated as

$$N(E) = \frac{8.0525(m+1)K}{\left[\left(\frac{T_{\text{max}}}{T_{\text{min}}} \right)^{m+1} - 1 \right]} \left(\frac{kT_{\text{min}}}{\text{keV}} \right)^{-2} I(E), \quad (4)$$

where

$$I(E) = \left(\frac{E}{kT_{\text{min}}} \right)^{m-1} \int_{\frac{E}{kT_{\text{max}}}}^{\frac{E}{kT_{\text{min}}}} \frac{x^{2-m}}{e^x - 1} dx, \quad (5)$$

and $x = E/kT$. Again, $N(E)$ is in units of $\text{ph cm}^{-2} \text{ s}^{-1} \text{ keV}^{-1}$.

Table 1: The fitting results of the time-resolved spectra of GRB 081221 with the BB model and the mBB model

Time (s)	A_1	kT (keV)	PGSTAT/dof	BIC	A_2	kT_{\min} (keV)	kT_{\max} (keV)	m	PGSTAT/dof	BIC
(0.00,2.00)	$0.69^{+0.03}_{-0.03}$	$30.72^{+1.64}_{-1.48}$	388.85/364	400.65	$2.03^{+2.16}_{-0.21}$	$3.74^{+5.13}_{-0.36}$	$79.32^{+26.08}_{-3.58}$	$0.25^{+0.05}_{-0.54}$	336.88/362	360.49
(2.00,4.00)	$0.65^{+0.02}_{-0.02}$	$16.44^{+0.64}_{-0.56}$	398.35/364	410.15	$3.56^{+0.66}_{-0.82}$	$5.64^{+1.78}_{-1.61}$	$54.88^{+17.04}_{-7.88}$	$-0.65^{+0.39}_{-0.43}$	308.02/362	331.63
(4.00,6.00)	$0.43^{+0.02}_{-0.03}$	$11.61^{+0.64}_{-0.56}$	365.33/364	377.12	$3.70^{+0.40}_{-0.08}$	$5.84^{+1.14}_{-0.24}$	$46.49^{+346.38}_{-13.07}$	$-1.31^{+0.18}_{-0.18}$	302.36/362	325.98
(6.00,8.00)	$0.24^{+0.03}_{-0.03}$	$9.65^{+0.73}_{-0.63}$	344.54/364	356.34	$3.47^{+0.31}_{-0.28}$	$5.49^{+0.86}_{-0.68}$	$364.53^{+493.58}_{-142.56}$	$-1.54^{+0.17}_{-0.29}$	313.94/362	337.55
(8.00,10.00)	$0.29^{+0.03}_{-0.03}$	$10.21^{+0.64}_{-0.59}$	299.41/364	311.20	$3.01^{+0.34}_{-0.34}$	$4.42^{+0.85}_{-0.85}$	$36.11^{+338.91}_{-16.54}$	$-1.16^{+0.23}_{-0.23}$	267.90/362	291.51
(10.00,12.00)	$0.14^{+0.03}_{-0.03}$	$7.16^{+0.53}_{-0.46}$	332.47/364	344.27	$3.03^{+0.14}_{-0.49}$	$4.36^{+0.35}_{-0.96}$	$106.22^{+345.39}_{-99.35}$	$-1.81^{+0.29}_{-0.11}$	317.17/362	340.78
(12.00,14.00)	$0.21^{+0.03}_{-0.03}$	$9.80^{+0.84}_{-0.65}$	328.09/364	339.89	$2.91^{+0.47}_{-0.53}$	$4.33^{+1.08}_{-0.96}$	$157.80^{+331.54}_{-118.79}$	$-1.19^{+0.15}_{-0.24}$	284.23/362	307.84
(14.00,16.00)	$0.50^{+0.02}_{-0.02}$	$10.21^{+0.44}_{-0.42}$	350.09/364	361.89	$2.07^{+0.36}_{-0.36}$	$2.62^{+0.76}_{-0.76}$	$33.91^{+378.53}_{-7.64}$	$-0.73^{+0.21}_{-0.21}$	267.42/362	291.04
(16.00,17.00)	$0.44^{+0.03}_{-0.03}$	$9.02^{+0.72}_{-0.66}$	370.33/364	382.13	$2.83^{+0.58}_{-0.23}$	$3.58^{+1.17}_{-0.36}$	$64.27^{+366.77}_{-34.99}$	$-1.29^{+0.09}_{-0.30}$	317.60/362	341.21
(17.00,18.00)	$0.88^{+0.02}_{-0.02}$	$15.35^{+0.54}_{-0.53}$	478.32/364	490.12	$1.39^{+0.02}_{-0.02}$	$1.87^{+2.14}_{-0.02}$	$52.40^{+11.31}_{-2.74}$	$-0.33^{+0.01}_{-0.32}$	317.05/362	340.66
(18.00,18.50)	$1.16^{+0.02}_{-0.02}$	$19.99^{+0.66}_{-0.55}$	329.25/364	341.05	$1.17^{+1.22}_{-0.39}$	$1.98^{+2.28}_{-0.24}$	$44.59^{+12.58}_{-1.20}$	$0.42^{+0.37}_{-0.37}$	261.68/362	285.29
(18.50,19.00)	$1.26^{+0.02}_{-0.02}$	$20.63^{+0.58}_{-0.56}$	370.22/364	382.02	$3.61^{+1.03}_{-0.02}$	$5.01^{+2.52}_{-0.04}$	$55.19^{+8.85}_{-2.83}$	$-0.06^{+0.06}_{-0.45}$	260.35/362	283.96
(19.00,19.50)	$1.28^{+0.01}_{-0.02}$	$21.29^{+0.60}_{-0.60}$	361.55/364	373.35	$3.15^{+0.88}_{-0.75}$	$4.33^{+2.27}_{-1.16}$	$50.38^{+14.58}_{-1.56}$	$0.30^{+0.38}_{-0.45}$	262.67/362	286.28
(19.50,20.00)	$1.24^{+0.02}_{-0.02}$	$19.93^{+0.52}_{-0.50}$	314.17/364	325.97	$2.97^{+0.92}_{-0.80}$	$4.12^{+2.42}_{-1.19}$	$38.11^{+8.36}_{-5.50}$	$0.61^{+0.38}_{-0.67}$	245.89/362	269.50
(20.00,20.50)	$1.27^{+0.02}_{-0.02}$	$20.09^{+0.57}_{-0.51}$	397.53/364	409.32	$3.36^{+0.67}_{-0.67}$	$4.46^{+2.29}_{-1.06}$	$54.78^{+7.30}_{-4.99}$	$-0.04^{+0.18}_{-0.40}$	269.52/362	293.13
(20.50,21.00)	$1.35^{+0.01}_{-0.01}$	$21.47^{+0.54}_{-0.57}$	473.93/364	485.73	$2.97^{+0.62}_{-0.11}$	$3.80^{+1.41}_{-0.18}$	$55.92^{+12.07}_{-0.64}$	$0.14^{+0.26}_{-0.26}$	314.18/362	337.79
(21.00,21.50)	$1.43^{+0.03}_{-0.01}$	$22.38^{+0.50}_{-0.46}$	405.52/364	417.32	$2.46^{+0.80}_{-0.21}$	$3.18^{+1.55}_{-0.39}$	$48.25^{+5.50}_{-5.50}$	$0.48^{+0.26}_{-0.26}$	254.51/362	278.12
(21.50,22.00)	$1.42^{+0.01}_{-0.01}$	$21.35^{+0.48}_{-0.41}$	384.52/364	396.32	$2.30^{+0.91}_{-0.18}$	$3.05^{+1.93}_{-0.28}$	$40.79^{+9.23}_{-1.35}$	$0.70^{+0.26}_{-0.32}$	284.85/362	308.46
(22.00,22.50)	$1.32^{+0.01}_{-0.01}$	$19.44^{+0.48}_{-0.45}$	421.93/364	433.73	$2.75^{+1.83}_{-0.27}$	$3.40^{+3.62}_{-0.95}$	$48.13^{+11.45}_{-2.12}$	$0.14^{+0.06}_{-0.70}$	268.20/362	291.81
(22.50,23.00)	$1.22^{+0.01}_{-0.02}$	$18.53^{+0.57}_{-0.48}$	348.99/364	360.79	$1.60^{+1.03}_{-0.71}$	$2.13^{+1.58}_{-0.58}$	$46.69^{+9.11}_{-1.62}$	$0.17^{+0.02}_{-0.50}$	234.22/362	257.83
(23.00,23.50)	$1.18^{+0.02}_{-0.02}$	$16.54^{+0.53}_{-0.49}$	389.35/364	401.15	$4.35^{+0.31}_{-0.45}$	$6.29^{+0.87}_{-1.10}$	$63.59^{+8.37}_{-0.73}$	$-0.82^{+0.21}_{-0.21}$	218.00/362	241.61
(23.50,24.00)	$1.26^{+0.01}_{-0.01}$	$18.46^{+0.54}_{-0.46}$	412.20/364	424.00	$3.06^{+0.16}_{-0.16}$	$3.79^{+0.26}_{-0.26}$	$53.81^{+2.11}_{-2.11}$	$-0.12^{+0.41}_{-0.41}$	256.61/362	280.22
(24.00,24.50)	$1.36^{+0.01}_{-0.01}$	$20.43^{+0.49}_{-0.50}$	414.72/364	426.52	$3.47^{+0.86}_{-1.08}$	$4.51^{+1.86}_{-1.58}$	$55.93^{+6.89}_{-5.05}$	$-0.05^{+0.23}_{-0.33}$	238.71/362	262.32
(24.50,25.00)	$1.28^{+0.01}_{-0.02}$	$17.85^{+0.42}_{-0.42}$	435.96/364	447.76	$4.05^{+0.45}_{-0.65}$	$5.53^{+1.12}_{-1.30}$	$55.18^{+6.54}_{-4.96}$	$-0.47^{+0.26}_{-0.24}$	262.46/362	286.07
(25.00,25.50)	$1.16^{+0.02}_{-0.02}$	$15.16^{+0.47}_{-0.40}$	434.11/364	445.91	$2.30^{+1.25}_{-0.63}$	$2.51^{+1.84}_{-0.62}$	$47.81^{+6.95}_{-3.07}$	$-0.35^{+0.09}_{-0.30}$	268.31/362	291.92
(25.50,26.00)	$1.16^{+0.01}_{-0.02}$	$14.18^{+0.39}_{-0.41}$	360.71/364	372.51	$1.80^{+0.80}_{-0.23}$	$2.09^{+1.17}_{-0.26}$	$36.18^{+6.04}_{-1.69}$	$-0.07^{+0.02}_{-0.54}$	241.03/362	264.64
(26.00,26.50)	$1.15^{+0.02}_{-0.02}$	$13.20^{+0.40}_{-0.36}$	390.14/364	401.94	$4.47^{+0.45}_{-0.19}$	$6.27^{+1.31}_{-0.49}$	$51.84^{+190.77}_{-3.05}$	$-1.19^{+0.11}_{-0.44}$	254.73/362	278.34
(26.50,27.00)	$1.15^{+0.01}_{-0.01}$	$13.18^{+0.33}_{-0.36}$	417.67/364	429.47	$1.83^{+1.60}_{-0.02}$	$2.02^{+1.98}_{-0.04}$	$35.13^{+5.61}_{-1.29}$	$-0.20^{+0.02}_{-0.43}$	278.27/362	301.88
(27.00,27.50)	$1.16^{+0.02}_{-0.02}$	$12.86^{+0.40}_{-0.35}$	406.79/364	418.59	$4.38^{+0.35}_{-0.33}$	$5.93^{+0.99}_{-0.77}$	$55.82^{+17.44}_{-6.50}$	$-1.21^{+0.22}_{-0.26}$	250.26/362	273.88
(27.50,28.00)	$1.13^{+0.02}_{-0.02}$	$13.33^{+0.46}_{-0.43}$	452.96/364	464.75	$3.58^{+0.41}_{-0.66}$	$4.24^{+0.84}_{-1.07}$	$55.57^{+8.64}_{-6.24}$	$-0.85^{+0.22}_{-0.18}$	252.09/362	275.70
(28.00,28.50)	$1.09^{+0.02}_{-0.02}$	$12.98^{+0.45}_{-0.41}$	417.06/364	428.86	$3.63^{+0.51}_{-0.38}$	$4.39^{+1.09}_{-0.69}$	$53.55^{+12.81}_{-4.45}$	$-0.87^{+0.14}_{-0.27}$	253.16/362	276.77
(28.50,29.00)	$1.08^{+0.02}_{-0.02}$	$13.19^{+0.49}_{-0.48}$	396.99/364	408.79	$3.38^{+0.59}_{-0.38}$	$3.96^{+1.14}_{-0.59}$	$50.39^{+10.44}_{-4.12}$	$-0.77^{+0.13}_{-0.14}$	235.18/362	258.79
(29.00,29.50)	$1.03^{+0.02}_{-0.02}$	$13.20^{+0.55}_{-0.52}$	398.43/364	410.24	$3.44^{+0.50}_{-0.45}$	$4.13^{+1.04}_{-0.75}$	$62.45^{+15.85}_{-6.83}$	$-0.86^{+0.14}_{-0.21}$	232.75/362	256.36
(29.50,30.00)	$1.01^{+0.02}_{-0.02}$	$12.45^{+0.53}_{-0.46}$	362.23/364	374.04	$3.61^{+0.51}_{-0.49}$	$4.47^{+1.08}_{-0.86}$	$46.57^{+10.44}_{-5.27}$	$-0.91^{+0.19}_{-0.32}$	245.11/362	268.72
(30.00,30.50)	$0.97^{+0.02}_{-0.02}$	$12.58^{+0.49}_{-0.48}$	335.44/364	347.24	$3.56^{+0.72}_{-0.50}$	$4.44^{+1.64}_{-0.87}$	$52.72^{+46.95}_{-8.14}$	$-0.94^{+0.24}_{-0.43}$	233.09/362	256.70
(30.50,31.00)	$0.91^{+0.02}_{-0.02}$	$11.69^{+0.58}_{-0.54}$	376.28/364	388.08	$3.61^{+0.67}_{-0.15}$	$4.55^{+1.58}_{-0.30}$	$56.60^{+405.12}_{-3.49}$	$-1.07^{+0.06}_{-0.44}$	276.00/362	299.61
(31.00,31.50)	$0.86^{+0.02}_{-0.02}$	$11.57^{+0.55}_{-0.51}$	283.93/364	295.73	$3.94^{+0.60}_{-0.01}$	$5.39^{+1.63}_{-0.08}$	$43.76^{+369.45}_{-15.08}$	$-1.22^{+0.24}_{-0.24}$	228.62/362	252.23
(31.50,33.60)	$0.74^{+0.01}_{-0.01}$	$11.30^{+0.33}_{-0.34}$	382.33/364	394.13	$3.04^{+1.06}_{-0.45}$	$3.86^{+2.19}_{-0.65}$	$35.49^{+20.33}_{-1.99}$	$-0.77^{+0.18}_{-0.75}$	271.64/362	295.25
(33.60,35.20)	$0.54^{+0.02}_{-0.02}$	$9.78^{+0.41}_{-0.42}$	383.78/364	395.58	$3.35^{+0.23}_{-0.23}$	$4.53^{+0.59}_{-0.59}$	$38.59^{+378.53}_{-11.85}$	$-1.29^{+0.17}_{-0.17}$	312.56/362	336.17
(35.20,40.00)	$0.27^{+0.02}_{-0.02}$	$8.99^{+0.34}_{-0.31}$	340.80/364	352.60	$3.64^{+0.05}_{-0.26}$	$5.76^{+0.15}_{-0.68}$	$849.34^{+150.64}_{-317.78}$	$-1.92^{+0.21}_{-0.03}$	297.39/362	321.00

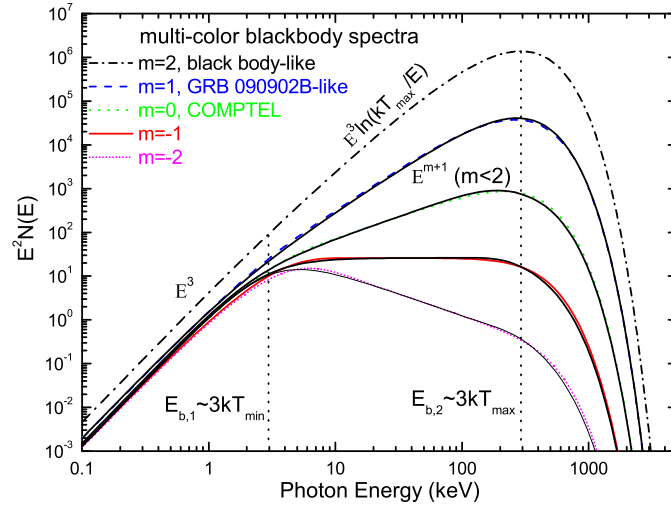


Fig. 1.— Examples of the mBB spectra for different m . $kT_{\min} = 1$ keV and $kT_{\max} = 100$ keV are assumed. Black solid lines are plotted with analytic approximations Eq. (6), while other lines are exact numerical calculations with Eq. (4).

Table 2: The fitting results of the time-integrated spectrum of GRB 081221 from 20 s to 30 s using mBB and Band function model

mBB model				
kT_{\min} (keV)	kT_{\max} (keV)	m	PGSTAT/dof	BIC
4.4 ± 0.3	$57.0^{+1.6}_{-1.4}$	$-0.46^{+0.05}_{-0.06}$	484.2/362	507.8
Band function model				
α	β	E_p	PGSTAT/dof	BIC
-0.60 ± 0.03	$-3.3^{+0.1}_{-0.2}$	$90.1^{+1.6}_{-1.2}$	468.1/362	491.7

Table 3. The comparison of the BIC for the time-resolved spectral fitting of GRB 081221 with the BB, the mBB and the 2BBPL models

Time	BIC _{BB}	BIC _{mBB}	BIC _{2BBPL}	BIC _{mBB} - BIC _{BB}	BIC _{2BBPL} - BIC _{BB}
0.00~0.67	256.05	265.93	276.29	9.88	20.24
0.67~0.77	163.06	174.96	186.09	11.90	23.03
0.77~0.87	146.14	158.49	169.80	12.35	23.66
0.87~0.97	132.97	144.91	156.45	11.94	23.48
0.97~1.07	154.86	166.57	178.07	11.71	23.21
1.07~1.17	159.68	171.59	183.08	11.91	23.40
1.17~1.27	166.20	179.41	189.74	13.21	23.54
1.27~1.37	153.06	164.81	176.52	11.75	23.46
1.37~1.47	160.48	172.48	183.82	11.99	23.33
1.47~1.57	166.02	176.93	189.38	10.91	23.36
1.57~1.67	155.17	168.85	178.64	13.68	23.47
1.67~1.77	142.25	154.01	165.73	11.76	23.48
1.77~1.87	142.53	154.27	165.90	11.74	23.37
1.87~1.97	148.46	162.00	171.95	13.55	23.50
1.97~2.07	131.41	141.83	154.16	10.42	22.75
2.07~2.17	127.25	138.93	150.73	11.69	23.48
2.17~2.27	134.52	144.83	156.27	10.31	21.75
2.27~2.37	144.38	156.05	166.83	11.67	22.45
2.37~2.47	152.27	163.91	175.74	11.65	23.48
2.47~2.57	151.96	163.37	173.70	11.40	21.73
2.57~2.67	138.23	150.16	161.57	11.93	23.34
2.67~2.77	139.66	150.58	162.34	10.92	22.68
2.77~2.87	150.93	162.21	174.41	11.28	23.48
2.87~2.97	166.39	177.64	188.73	11.25	22.34
2.97~3.07	151.20	162.62	174.47	11.41	23.26
3.07~3.17	148.46	160.01	171.94	11.56	23.48
3.17~3.27	147.78	159.31	171.26	11.53	23.49
3.27~3.37	136.96	148.69	160.46	11.73	23.50
3.37~3.47	136.30	147.95	159.81	11.64	23.51
3.47~3.57	164.98	176.69	188.46	11.71	23.49
3.57~3.67	131.49	143.23	154.99	11.74	23.50
3.67~3.77	138.22	149.92	161.71	11.69	23.49
3.77~3.87	160.07	171.02	183.32	10.95	23.25
3.87~3.97	161.91	173.64	185.39	11.73	23.48
3.97~4.07	151.72	163.42	175.09	11.70	23.37
4.07~4.67	275.38	271.56	285.75	-3.82	10.37
4.67~5.33	251.75	253.43	263.59	1.68	11.84
5.33~6.00	282.56	280.57	292.08	-1.99	9.52
6.00~6.67	255.33	253.63	264.14	-1.70	8.81
6.67~7.33	252.66	263.44	275.24	10.78	22.58
7.33~8.00	255.57	264.88	276.96	9.31	21.39
8.00~8.67	259.47	265.78	276.88	6.31	17.41
8.67~9.33	253.04	254.60	267.35	1.56	14.31
9.33~10.00	242.98	246.50	258.32	3.52	15.34
10.00~10.67	243.74	250.10	261.68	6.36	17.94
10.67~11.34	247.07	256.10	267.65	9.03	20.58
11.34~12.00	253.76	264.03	275.12	10.27	21.36
12.00~12.67	235.10	243.46	254.82	8.36	19.72
12.67~15.33	266.91	277.31	288.49	10.40	21.58
15.33~15.67	208.43	211.10	221.19	2.67	12.76
15.67~16.00	213.91	218.08	231.27	4.17	17.36
16.00~16.10	119.25	130.61	142.52	11.36	23.27
16.10~16.20	138.01	149.75	161.48	11.74	23.47
16.20~16.30	140.26	151.77	163.77	11.51	23.51
16.30~16.40	159.18	170.90	182.68	11.72	23.50
16.40~16.50	140.37	151.37	163.48	11.00	23.12
16.50~16.60	139.87	151.60	163.38	11.73	23.51
16.60~16.70	139.70	150.85	163.20	11.14	23.49
16.70~16.80	136.73	148.04	160.21	11.31	23.49
16.80~16.90	144.63	156.05	168.11	11.43	23.49
16.90~17.00	152.34	163.17	174.81	10.83	22.46
17.00~17.10	160.83	171.36	183.09	10.53	22.25
17.10~17.20	128.09	139.85	149.42	11.76	21.33
17.20~17.30	158.65	165.57	177.83	6.92	19.18
17.30~17.40	144.31	152.10	164.05	7.79	19.74
17.40~17.50	158.98	167.83	176.23	8.85	17.25
17.50~17.60	145.35	150.76	163.09	5.41	17.75

Table 3—Continued

Tine	BIC _{BB}	BIC _{mBB}	BIC _{2BBPL}	BIC _{mBB} - BIC _{BB}	BIC _{2BBPL} - BIC _{BB}
17.60~17.70	172.41	177.77	189.15	5.36	16.74
17.70~17.80	176.06	176.37	188.14	0.31	12.08
17.80~17.90	189.64	198.03	210.22	8.39	20.58
17.90~18.00	191.48	199.89	211.45	8.40	19.97
18.00~18.10	184.69	189.73	198.57	5.04	13.88
18.10~18.20	187.04	194.63	201.79	7.59	14.75
18.20~18.30	156.25	165.17	176.39	8.92	20.13
18.30~18.40	203.47	210.40	224.38	6.94	20.92
18.40~18.50	175.11	174.00	183.14	-1.11	8.03
18.50~18.60	209.72	211.57	223.23	1.86	13.51
18.60~18.70	151.38	158.14	168.22	6.76	16.84
18.70~18.80	238.87	235.80	245.64	-3.07	6.76
18.80~18.90	202.84	211.46	220.62	8.62	17.78
18.90~19.00	190.99	180.60	192.22	-10.39	1.24
19.00~19.10	170.73	175.92	186.47	5.19	15.74
19.10~19.20	205.92	208.74	220.56	2.82	14.64
19.20~19.30	220.96	213.03	223.20	-7.93	2.24
19.30~19.40	184.45	188.62	201.18	4.17	16.73
19.40~19.50	172.91	179.04	188.86	6.14	15.95
19.50~19.60	188.42	184.51	191.64	-3.91	3.22
19.60~19.70	196.12	206.00	219.07	9.88	22.95
19.70~19.80	154.11	156.86	166.20	2.75	12.09
19.80~19.90	171.93	181.54	194.16	9.61	22.23
19.90~20.00	182.33	188.80	202.42	6.47	20.09
20.00~20.10	178.06	177.95	186.95	-0.11	8.89
20.10~20.20	208.05	203.65	209.37	-4.39	1.32
20.20~20.30	218.22	214.45	224.90	-3.78	6.68
20.30~20.40	233.46	223.39	234.59	-10.07	1.13
20.40~20.50	207.90	212.39	222.89	4.48	14.98
20.50~20.60	222.75	199.74	208.77	-23.01	-13.97
20.60~20.70	204.40	196.08	209.56	-8.32	5.16
20.70~20.80	226.36	219.33	232.11	-7.02	5.76
20.80~20.90	203.05	209.95	221.64	6.90	18.59
20.90~21.00	220.08	207.14	214.90	-12.94	-5.18
21.00~21.10	207.37	207.83	214.21	0.46	6.84
21.10~21.20	191.65	177.20	189.19	-14.45	-2.46
21.20~21.30	187.38	181.57	190.85	-5.81	3.47
21.30~21.40	203.11	191.11	204.61	-12.00	1.50
21.40~21.50	198.27	189.27	200.72	-9.00	2.45
21.50~21.60	188.64	177.99	187.01	-10.66	-1.63
21.60~21.70	182.86	186.65	198.93	3.79	16.07
21.70~21.80	183.93	188.65	200.60	4.72	16.67
21.80~21.90	208.08	204.34	216.54	-3.74	8.46
21.90~22.00	197.73	202.44	206.14	4.71	8.41
22.00~22.10	217.01	214.35	220.98	-2.65	3.97
22.10~22.20	212.97	198.48	207.70	-14.49	-5.27
22.20~22.30	181.44	161.99	169.98	-19.45	-11.46
22.30~22.40	174.37	175.94	186.64	1.57	12.27
22.40~22.50	193.43	191.49	202.23	-1.94	8.79
22.50~22.60	174.69	177.55	184.81	2.86	10.12
22.60~22.70	154.70	159.05	171.59	4.35	16.89
22.70~22.80	170.25	178.47	190.53	8.22	20.29
22.80~22.90	194.25	181.45	192.00	-12.81	-2.25
22.90~23.00	174.42	169.57	182.26	-4.85	7.84
23.00~23.10	194.12	187.35	197.52	-6.77	3.40
23.10~23.20	193.26	189.46	200.54	-3.79	7.29
23.20~23.30	203.06	194.53	204.17	-8.53	1.11
23.30~23.40	180.35	172.15	183.64	-8.21	3.28
23.40~23.50	170.61	160.44	170.03	-10.16	-0.58
23.50~23.60	202.59	205.74	210.93	3.15	8.34
23.60~23.70	237.94	233.49	247.12	-4.45	9.18
23.70~23.80	190.02	180.35	190.95	-9.68	0.92
23.80~23.90	184.72	186.09	199.21	1.37	14.49
23.90~24.00	196.14	177.51	188.94	-18.64	-7.20
24.00~24.10	199.37	195.83	207.68	-3.54	8.32
24.10~24.20	190.29	193.12	202.97	2.83	12.68
24.20~24.30	226.08	202.10	215.47	-23.98	-10.60

Table 3—Continued

Tine	BIC _{BB}	BIC _{mBB}	BIC _{2BBPL}	BIC _{mBB} - BIC _{BB}	BIC _{2BBPL} - BIC _{BB}
24.30~24.40	216.09	199.08	212.84	-17.01	-3.26
24.40~24.50	196.75	181.18	189.75	-15.57	-7.00
24.50~24.60	216.32	205.19	213.01	-11.13	-3.31
24.60~24.70	213.81	195.80	210.60	-18.01	-3.21
24.70~24.80	194.98	185.41	195.29	-9.57	0.31
24.80~24.90	147.48	142.97	153.20	-4.51	5.72
24.90~25.00	183.59	175.05	187.22	-8.53	3.64
25.00~25.10	231.76	215.88	226.04	-15.88	-5.72
25.10~25.20	189.87	179.70	190.21	-10.16	0.34
25.20~25.30	172.13	171.41	183.89	-0.71	11.76
25.30~25.40	169.01	168.62	181.44	-0.40	12.43
25.40~25.50	179.88	173.96	184.37	-5.92	4.49
25.50~25.60	191.94	197.37	210.59	5.43	18.65
25.60~25.70	175.34	165.55	177.74	-9.79	2.41
25.70~25.80	183.28	185.36	195.75	2.08	12.47
25.80~25.90	213.34	217.37	228.02	4.04	14.69
25.90~26.00	163.26	164.65	174.48	1.39	11.22
26.00~26.10	151.56	154.81	167.56	3.25	16.00
26.10~26.20	197.51	187.90	198.73	-9.61	1.22
26.20~26.30	197.78	194.71	205.45	-3.08	7.67
26.30~26.40	214.50	205.95	215.38	-8.55	0.88
26.40~26.50	164.50	172.61	184.13	8.11	19.63
26.50~26.60	189.09	191.87	203.49	2.78	14.40
26.60~26.70	188.40	183.74	196.51	-4.65	8.11
26.70~26.80	158.44	159.42	173.14	0.97	14.69
26.80~26.90	184.99	187.09	199.69	2.10	14.70
26.90~27.00	190.92	187.11	200.57	-3.81	9.65
27.00~27.10	170.08	174.78	188.70	4.70	18.62
27.10~27.20	162.90	166.33	179.19	3.43	16.29
27.20~27.30	190.46	186.73	197.17	-3.72	6.72
27.30~27.40	183.42	177.64	189.68	-5.79	6.26
27.40~27.50	194.24	180.25	192.88	-13.99	-1.35
27.50~27.60	203.85	196.77	205.84	-7.08	1.98
27.60~27.70	181.29	162.55	171.49	-18.74	-9.80
27.70~27.80	200.48	186.88	197.85	-13.60	-2.63
27.80~27.90	180.43	167.74	176.31	-12.70	-4.12
27.90~28.00	174.39	168.61	179.39	-5.78	5.00
28.00~28.10	197.94	194.10	205.03	-3.84	7.09
28.10~28.20	198.42	186.08	202.35	-12.35	3.93
28.20~28.30	188.50	185.48	198.93	-3.02	10.43
28.30~28.40	194.75	199.06	210.73	4.31	15.98
28.40~28.50	195.05	187.07	199.93	-7.99	4.87
28.50~28.60	162.56	158.44	167.76	-4.12	5.20
28.60~28.70	194.32	184.54	196.62	-9.77	2.31
28.70~28.80	166.64	158.21	172.29	-8.43	5.66
28.80~28.90	159.29	160.38	172.09	1.09	12.80
28.90~29.00	189.64	188.83	201.01	-0.82	11.36
29.00~29.10	204.35	201.13	212.66	-3.21	8.31
29.10~29.20	201.35	201.25	213.75	-0.11	12.40
29.20~29.30	163.01	163.79	175.65	0.78	12.64
29.30~29.40	190.09	182.91	191.79	-7.18	1.70
29.40~29.50	193.32	187.47	201.17	-5.84	7.86
29.50~29.60	162.99	168.64	180.78	5.65	17.78
29.60~29.70	161.95	166.78	181.59	4.83	19.64
29.70~29.80	145.50	145.11	156.84	-0.40	11.34
29.80~29.90	186.67	183.41	194.42	-3.26	7.75
29.90~30.00	164.27	170.06	185.06	5.79	20.79
30.00~30.10	170.41	180.75	192.99	10.34	22.58
30.10~30.20	190.23	184.10	196.93	-6.13	6.70
30.20~30.30	169.75	178.41	190.35	8.66	20.60
30.30~30.40	162.25	167.36	178.78	5.11	16.53
30.40~30.50	179.54	180.13	189.30	0.59	9.76
30.50~30.60	171.23	172.59	184.03	1.36	12.80
30.60~30.70	150.37	154.99	168.70	4.61	18.33
30.70~30.80	182.95	184.85	195.79	1.90	12.84
30.80~30.90	197.42	202.28	215.48	4.86	18.06
30.90~31.00	158.36	167.72	179.28	9.37	20.93

Assuming $T_{\min} \ll T_{\max}$ and $m < 2$, $I(E)$ can be approximated to

$$I(E) \approx \begin{cases} \frac{1}{2-m} \left(\frac{E}{kT_{\min}} \right), & E \ll kT_{\min} \\ \Gamma(3-m)\zeta(3-m) \left(\frac{E}{kT_{\min}} \right)^{m-1}, & kT_{\min} \ll E \ll kT_{\max} \\ \left(\frac{T_{\min}}{T_{\max}} \right)^{2-m} \left(\frac{E}{kT_{\min}} \right) e^{-\frac{E}{kT_{\max}}}, & kT_{\max} \ll E \end{cases} \quad (6)$$

where $\Gamma(x)$ and $\zeta(x)$ are the Gamma function and Zeta function, respectively. The above equation shows that the low energy ($E \ll kT_{\min}$) photon spectrum follows the Rayleigh-Jeans law of $N(E) \propto E$, while the high energy ($E \gg kT_{\max}$) spectrum behaves as a power law with an exponential cutoff. For the middle regime of the spectrum ($kT_{\min} < E < kT_{\max}$), different m corresponds to different shape. We can see that $m \leq 2$ is required. Otherwise, the photon spectrum $N(E) \propto E^{m-1}$ in the energy band of $kT_{\min} < E < kT_{\max}$ is harder than the blackbody $N(E) \propto E$, which is physically unrealistic. In fact, for $m > 2$, $N(E)$ is always proportional to E for $E < kT_{\max}$, as in this case the whole spectrum is dominated by the $T = T_{\max}$ blackbody. Thus compared with Ryde et al. (2010), by considering the effect of T_{\min} , we obtain the complete mBB spectrum including the Rayleigh-Jeans component ($E < kT_{\min}$).

In Figure 1, we plot the mBB spectra for different m values. $kT_{\min} = 1$ keV and $kT_{\max} = 100$ keV are assumed. For $m = 2$, the spectrum is similar to a pure blackbody. In the $E^2 N(E)$ spectrum, however, it deviates from the pure blackbody by a factor of $\ln(kT_{\max}/E)$ from kT_{\min} to kT_{\max} . Note that for $m = 2$ the low energy spectrum of $E < 3kT_{\min}$ is influenced by the entire black body components with temperatures from kT_{\min} to kT_{\max} , while the low energy spectrum is mainly dominated by the black body component with temperature $\sim kT_{\min}$ for $m < 2$, which explains a higher $E^2 N(E)$ for the $m = 2$ case. The spectrum in the case of $m = 1$ can nicely explain the observed narrowly-shaped spectrum of GRB 090902B. For $m = 0$, it is the same as the Comptonized spectrum, which is also known as the COMPTEL model (Goldstein et al. 2012). As for GRB 081221 analyzed in the next section, the spectrum ($m = -0.46$) is between the two cases of $m = 0$ and $m = -1$. If the minimum and maximum temperatures are close enough, i.e., $T_{\min} \sim T_{\max}$, the spectrum returns to the pure blackbody. On the other hand, if the minimum temperature T_{\min} is below the energy band of the GRB detector, the low energy part of the mBB spectrum can not be observed, and the middle and the high energy parts might be approximated as the well-known Band spectrum or the Comptonized cut-off power law spectrum in a limited energy band determined by the detector. In this paper, we only consider the case of a single

Table 3—Continued

Tine	BIC _{BB}	BIC _{mBB}	BIC _{2BBPL}	BIC _{mBB} - BIC _{BB}	BIC _{2BBPL} - BIC _{BB}
31.00~31.10	154.39	165.78	177.60	11.39	23.21
31.10~31.20	143.08	146.60	159.93	3.52	16.86
31.20~31.30	159.00	167.74	179.31	8.73	20.31
31.30~31.40	165.01	174.76	187.35	9.76	22.35
31.40~31.50	159.08	168.24	179.00	9.16	19.92
31.50~31.60	168.77	176.52	188.76	7.75	19.99
31.60~31.70	148.84	155.02	169.39	6.18	20.55
31.70~31.80	155.60	161.41	172.84	5.81	17.23
31.80~31.90	147.21	157.40	170.39	10.19	23.17
31.90~32.00	148.55	159.74	171.84	11.19	23.29
32.00~32.10	138.15	149.59	161.64	11.44	23.49
32.10~32.20	164.11	175.00	185.58	10.90	21.47
32.20~32.30	138.54	146.32	154.47	7.78	15.93
32.30~32.40	157.70	168.89	178.56	11.18	20.86
32.40~32.50	163.62	174.65	186.63	11.03	23.01
32.50~32.60	142.35	153.73	165.78	11.38	23.42
32.60~32.70	153.93	165.21	177.38	11.29	23.45
32.70~32.80	141.57	153.35	163.56	11.78	21.99
32.80~32.90	122.22	132.83	142.56	10.61	20.34
32.90~33.00	150.76	161.09	173.66	10.33	22.90
33.00~33.10	147.01	158.06	170.13	11.04	23.12
33.10~33.20	147.19	158.49	170.62	11.30	23.43
33.20~33.30	122.85	133.88	146.34	11.03	23.49
33.30~33.40	148.71	159.70	171.10	10.99	22.39
33.40~33.50	142.98	154.33	166.24	11.34	23.25
33.50~33.60	123.53	135.04	146.56	11.50	23.03
33.60~33.70	137.02	148.75	160.51	11.72	23.48
33.70~33.80	132.94	144.37	156.43	11.42	23.49
33.80~33.90	139.85	150.60	163.34	10.75	23.48
33.90~34.00	167.10	178.13	190.58	11.02	23.48
34.00~34.10	159.45	170.94	182.93	11.49	23.48
34.10~34.20	133.05	144.72	156.21	11.67	23.16
34.20~34.30	155.50	167.17	178.99	11.67	23.48
34.30~34.40	138.34	148.74	160.94	10.40	22.60
34.40~34.50	136.12	147.53	159.46	11.41	23.34
34.50~34.60	165.42	177.18	188.91	11.76	23.49
34.60~34.70	118.65	129.58	142.13	10.93	23.48
34.70~34.80	138.43	147.65	159.51	9.22	21.08
34.80~34.90	162.45	172.96	184.63	10.51	22.19
34.90~35.00	144.51	155.51	167.64	11.00	23.14
35.00~35.10	132.01	142.79	154.73	10.78	22.72
35.10~35.20	155.35	166.68	178.84	11.33	23.48
35.20~35.30	159.64	171.26	183.08	11.62	23.44
35.30~35.40	142.84	154.16	166.32	11.32	23.48
35.40~35.50	124.22	135.79	147.71	11.57	23.49
35.50~35.60	124.13	135.06	146.73	10.94	22.60
35.60~35.70	140.44	150.91	162.92	10.47	22.48
35.70~35.80	130.35	140.85	152.18	10.50	21.84

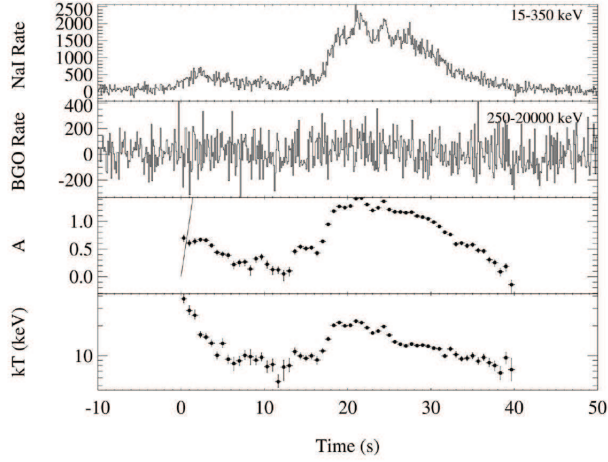


Fig. 2.— GBM light curves of GRB 081221 (top two panels), and the spectral evolution (bottom two panels).

power-law distribution of the blackbody temperature. The temperature distribution of more realistic GRB fireballs may be much complicated.

3. Spectral Analysis of GRB 081221

GRB 081221 at redshift $z = 2.26$ (Salvaterra et al. 2012), a bright GRB with separable pulses, was **detected** by Fermi/GBM, Swift/BAT, and Konus/Wind. There was no detection in the LAT band. We analyze the GBM data using the same method as described in Zhang et al. (2011) and fit the extracted spectra with McSpecFit package (Zhang et al 2016). We selected the data from GBM detectors NaI 1, NaI 2 and BGO 0, according to their geometry relative to the GRB position. The light curve with a duration of about 40 s consists of a weak initial peak (precursor) and a bright second peak (main burst), as can be seen in Figure 2. The duration of the precursor is about 5 s, and the quasi-quiescent time is ~ 10 s between these two peaks. The main burst consists of three overlapping pulses with a duration of ~ 20 seconds (Cummings et al. 2008; Golenetskii et al. 2008; Wilson-Hodge 2008). The event fluence of GRB 081221 is $(3.7 \pm 0.1) \times 10^{-5}$ erg cm $^{-2}$ (8-1000 keV), and the isotropic energy is $(4.21 \pm 0.42) \times 10^{52}$ erg.

We perform the time-resolved spectral analysis of GRB 081221 using the GBM data. We use the personal IDL code library ZBBIDL and personal Python library ZBBPY in the whole data processing project developed and applied in Zhang et al. (2018). Divided the

whole burst into 40 slices at first, we use a single blackbody (BB) model and an mBB model to fit the data, respectively. The fitting results are presented in Table 1. The Bayesian Information Criterion (BIC) is a tool for model selection (Schwarz 1978; Wei et al. 2016). A model is preferred when it has the lower BIC value than the other. We define $\Delta\text{BIC} = \text{BIC}_1 - \text{BIC}_2$, where BIC_i corresponds to Model i ($i = 1, 2$). If ΔBIC is from 2 to 6, the preference for Model 2 is positive; if ΔBIC is from 6 to 10, the preference for Model 2 is strong; and if ΔBIC is above 10, the preference for Model 2 is very strong. By comparing their BIC, we come to our conclusion that although the BB model is not the best-fit model, we can use this model to explore the physical properties of the GRB photosphere, and the BB model can be reasonably used to fit the data (Zhang et al. 2018). We also find when the weaker the radiation is, the more suitable the single blackbody model is. This means that the time slice with high fluence may be superimposed by a number of the BB components. The spectral evolution may be another important reason. We are then motivated to take a smaller time bin. Thanks to the high flux of this burst, we divide the burst into 250 slices based on the criterion that there are at least 20 net counts in at least 10 energy channels in the spectrum to conduct a fine-time-resolved spectral analysis. The two blackbodies plus a power-law model (2BBPL), which was applied to GRB 081221 by Basak & Rao (2013), is also considered in this work. The computed BIC for the time-resolved spectra of GRB 081221 with these three models are listed in Table 3. The evolution diagram of the ΔBIC with time and histogram about $\Delta\text{BIC}_{\text{mBB-BB}}$ and $\Delta\text{BIC}_{2\text{BBPL-BB}}$ are shown in Figure 3. The ΔBIC of most time intervals is larger than 10, so it can be judged that the single blackbody model is the best-fit model. Comparing the BIC values of the BB model in the Tables 1 and 3, we also find that the smaller the interval is, the more acceptable the single blackbody model is. It means that the whole radiation is superimposed with blackbodies of different temperature, and the spectral evolution has a great influence on the time-integrated spectrum. The temporal evolution of kT is shown in Figure 2. The kT of the precursor evolves quickly from ~ 30 keV to ~ 7 keV. In the main part of the burst, kT increases rapidly from ~ 9 keV to ~ 20 keV, then decreases with the flux.

The left panel of Figure 4 shows an example of a spectral fitting with a BB model in the interval of [19.5s, 20.0s], when the prompt emission is around the brightest peak, where we obtained $kT = 19.9 \pm 0.5$ keV. We noted the non-Gaussian pattern of the residuals indicate that the spectral evolution may still exist even within such a small time interval. Furthermore, the right panel of Figure 4 shows the flux - kT correlation for the time-resolved spectra, a higher flux generally corresponds to a BB component with a higher temperature (Golenetskii et al. 1983; Kargatis et al. 1994; Borgonovo & Ryde 2001; Fan et al. 2012). This is similar to the E_p -flux correlation in the Band model fittings (Lu et al. 2010). We fit the flux- kT data with a power-law for the decay phase of the second pulse ($t > 30$ s)

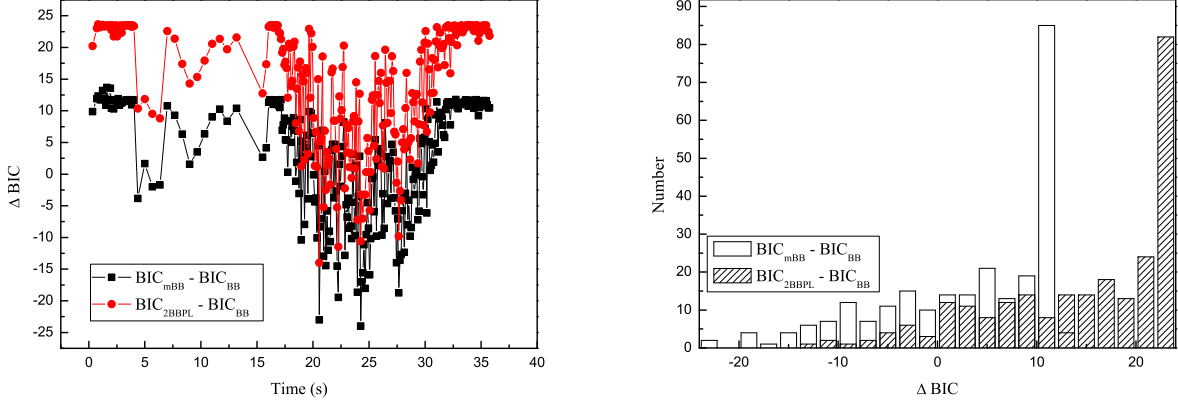


Fig. 3.— The evolution of the ΔBIC with time for the three models (left panel), and histogram of the ΔBIC (right panel).

and the time interval of 12 - 40s. The slopes are ~ 4.1 and ~ 2.7 , respectively. For the decay phase of the second pulse, this slope is consistent with the BB model prediction. For a BB, the luminosity of the photospheric emission is $L = 16\pi R^2 \frac{(1+z)^4}{\Gamma^2} \sigma T^4$, where R is the photospheric radius and Γ is the Lorentz factor. The luminosity is less sensitive to the radius ($\propto R^2$) and the Lorentz factor ($\propto \Gamma^{-2}$) than to the temperature ($\propto T^4$), so it is expected that the flux approximately proportional to T^4 . The deviation of the observed dependence of the BB flux on temperature ($T^{2.7}$) during the time interval of 12 - 40 s to the theoretical T^4 should be attributed to some mild temporal evolution of the photosphere radius and/or the Lorentz factor, as this time interval corresponds to the whole period of the main burst of GRB 081221, which consists of the rising, peak and decaying parts. Note that the slopes of 4.1 and 2.7 here are irrelevant with the power-law index m in Eq. (3).

The model fittings to the time-integrated GBM spectrum between 20 and 30 s of GRB 081221 are shown in Figure 5. Two spectral breaks at ~ 15 keV and ~ 180 keV are seen in this figure. The spectrum rises fast below ~ 15 keV, then shows a plateau segment between ~ 15 keV and ~ 180 keV, and finally follows a steep decrease above ~ 180 keV. The fitting results are presented in Table 2. Parameter constraints of the mBB model and Band function model for time-integrated spectrum between 20 and 30 s are shown in Fig.6. We find that the multi-color blackbody model ($m = -0.46$) can fit almost as well as the Band model, which means that the Band spectrum in GRB 081221 can be well interpreted as the mBB. The derived minimum and maximum temperatures ($kT_{\min} = 4.4 \pm 0.3$ keV, $kT_{\max} = 57.0^{+1.6}_{-1.4}$ keV) for the time-integrated spectrum. The derived single blackbody temperatures range from

12.45 $^{+0.53}_{-0.46}$ keV to 22.38 $^{+0.51}_{-0.46}$ keV. This difference can be understood by the following factors: (1) Different formulation. T_{\min} and T_{\max} can be regarded as effective temperatures which are not exactly the term of the temperature kT in the BB model. (2) Different selection of data. The first approach is applied to the whole time-integrated spectra while the 2nd approach is applied to each slice of the time-resolved spectra. So T_{\min} and T_{\max} in mBB are “averaged” values and are subject to spectral evolution. Thus they are not necessarily exactly as same as kT in the BB model.

Based on the above spectral analysis, we find that the prompt emission of GRB 081221 may be overwhelmed by the photospheric (thermal) emission, without any significant non-thermal contribution in the GBM energy band.

4. Discussion and Conclusions

Usually, the spectrum of thermal emission from astronomical objects can be described by the Planck function. However, for GRBs which are widely believed to have a relativistic outflow, due to the angle dependence of the photospheric emission together with the Doppler boosting effect (Pe’er 2008), the photospheric emission should be a superposition of blackbodies of different temperatures, which is also called the mBB.

We notice that, Ryde et al. (2010) and Larsson et al. (2011) used a broadened photospheric component based on an mBB model and the XSPEC model diskpbb to fit the spectra of GRB 090902B and GRB 061007, respectively. In their works, they adopted $T_{\min} \simeq 0$ as $T_{\min} \ll T_{\max}$ and kT_{\min} below the lowest energy of the energy band of the detector in their cases. In the diskbb model, the observed photon flux is given by

$$N(E) = \int_{T_{\text{out}}}^{T_{\text{in}}} \left(\frac{T}{T_{\text{in}}}\right)^m B(E, T) \frac{dT}{T_{\text{in}}}, \quad (7)$$

where the temperature of the outer edge of the disk can be regarded as $T_{\text{out}} = 0$. So the diskbb model is effectively the same as the model of Ryde et al. (2010), in which the temperature distribution is normalized by T_{\max} (T_{in} in the diskbb model).

It is worth pointing out that our model is slightly different from Ryde et al. (2010). In Ryde et al. (2010), they assumed a **probability distribution** of the mBB temperature. In our model, the distribution of the photosphere emission luminosity as a function of temperature is more directly related to the physics of the GRB fireball, and the power law index m of the distribution normalized by T_{\min} decides the shape of the low and middle energy part of the spectrum. If T_{\min} is small enough as to be outside the low-energy limit of the instrument, the observed spectrum becomes the Band or Comptonized cutoff power-law

spectrum. Otherwise, if T_{\min} is high enough as to be comparable to the T_{\max} , the observed spectrum is close to a pure blackbody.

In this paper, we systematically analyze the time-integrated and time-resolved spectra of the prompt emission of GRB 081221 based on the Fermi/GBM data. We find that the time-integrated spectrum is well fitted by the mBB model and the time-resolved spectra can be well fitted by the BB model (without any non-thermal power-law component), implying that the prompt emission of GRB 081221 may be dominated by the photospheric emission. Our results are summarized as follows:

- The time-integrated spectrum during the bright phase (from 20s to 30s since the trigger) of GRB 081221 observed with Fermi/GBM has a broad plateau in the 15-180 keV band, and is well fitted by the mBB model, yielding the $kT_{\min} = 4.4 \pm 0.3$ keV, $kT_{\max} = 57.0^{+1.6}_{-1.4}$ keV, $m = -0.46^{+0.05}_{-0.06}$.
- As for the time-resolved spectra, although the BB model is not the best-fit model when the whole burst is divided into 40 slices, we obtain acceptable fits with the single blackbody model (without the power-law component), which is simpler compared to the 2BB plus PL model of Basak & Rao (2013). The kT of the main burst increases rapidly from ~ 9 keV to ~ 20 keV. When the burst is divided into 250 slices, the BB model is much preferred than the Band model and the 2BB plus PL model, based on the Bayesian Information Criterion. This means that the evolution of the spectrum has a great influence on the time-integrated spectrum, and hence the time-binning greatly affects the theoretical interpretation of the observed time-integrated and even time-resolved spectra.

Our results indicate that the mBB should be the main intrinsic spectral component of GRB 081221, which is a superposition of a series of blackbodies with different temperatures arising at different times of the prompt phase. The identification of the photosphere origin of GRB 081221 suggests that the jet composition of this burst is a matter dominated fireball. On the other hand, the spectra of some bursts such as GRB 130606B (Zhang et al. 2016) are adequately modeled by the fast cooling synchrotron radiation model (Uhm & Zhang 2014), with no evidence of a thermal photosphere emission component, which suggests a Poynting-flux-dominated jet composition. The co-existence of both types of GRBs suggests that GRB jet composition is likely diverse, with different bursts having different degrees of magnetization from the central engine (e.g. Gao & Zhang 2015).

We appreciate the referee very much for his/her valuable comments and suggestions. We acknowledge the use of the public data from the Fermi data archives. This work

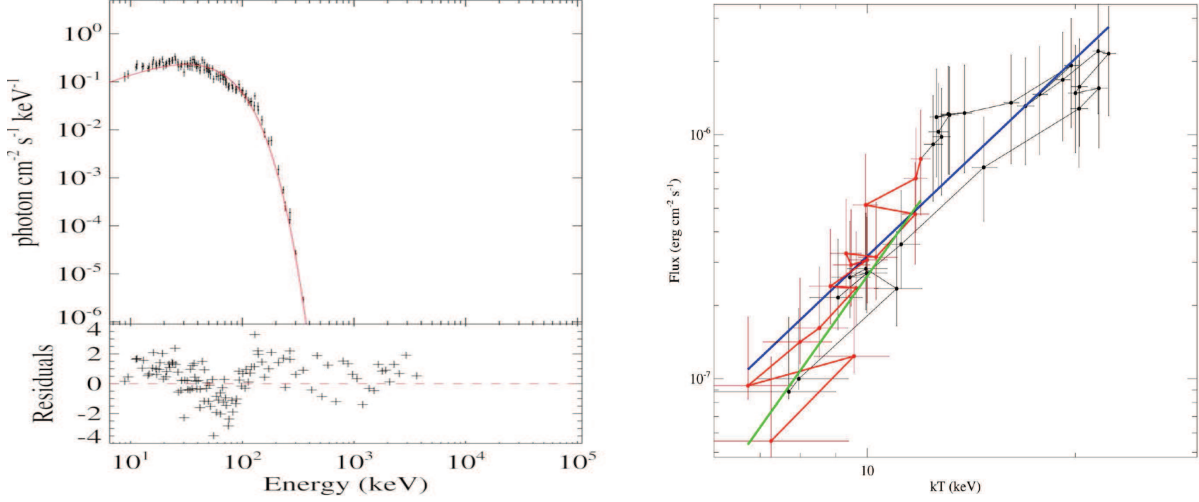


Fig. 4.— Left: the time resolved photon spectrum when the flux is around the highest peak (time from 19.5 s to 20.0 s since the trigger), in which a blackbody model is applied. Right: evolution of kT vs flux. The red points and green solid line indicate the data and the flux $\propto (kT)^{4.1}$ correlation in the decay phase of the second (main) pulse ($t > 30$ s). The blue solid line indicates the flux $\propto (kT)^{2.7}$ for the whole period of the second (main) pulse ($t = 12 - 40$ s).

was supported by the National Basic Research Program (973 Program) of China (Grants 2014CB845800), the National Natural Science Foundation of China (Grant Nos 11725314, 11673068, 11473022, 11503011, 11275057, 11543004, 11233006 and 11603006), the Open Research Program of Key Laboratory for the Structure and Evolution of Celestial Objects (OP201403 and OP201703), key scientific and technological project of Henan province (No.172102310334), the Key Research Program of Frontier Sciences (QYZDB-SSW-SYS005) and the Strategic Priority Research Program “multi-waveband gravitational wave Universe” (grant No. XDB23000000) of the Chinese Academy of Sciences, the Fundamental Research Funds for the Central Universities, Nanyang Normal University Doctoral Fund(15064) and the Key Scientific Research Project in Universities of Henan Province (Grant 15A160001). Part of this work used BBZ’s personal IDL code library ZBBIDL and personal Python library ZBBPY. The computation resources used in this work are owned by Scientist Support LLC.

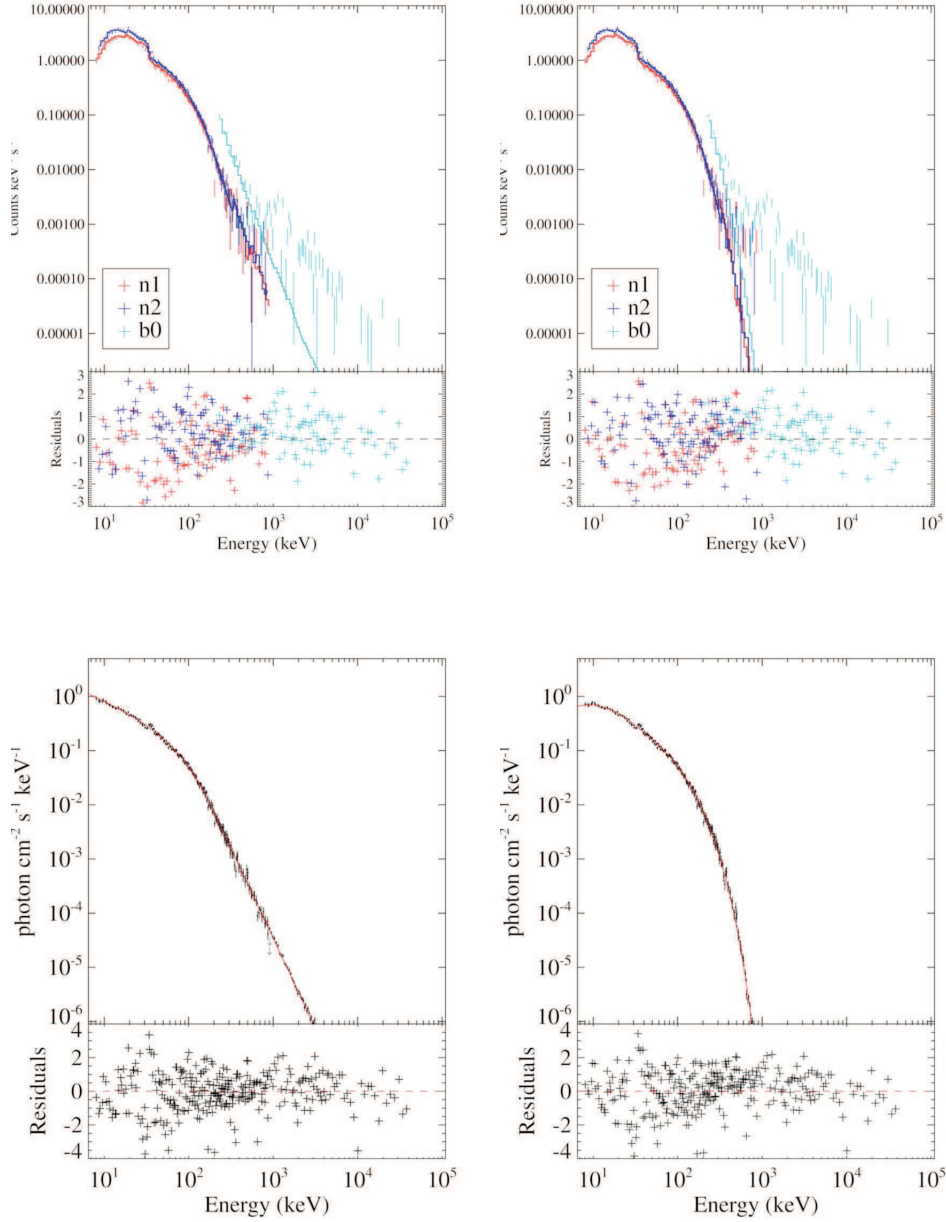


Fig. 5.— Comparison between the Band function fitting and the mBB model fitting for the time integrated spectrum between 20 and 30 s. The spectra have been re-binned into wider bins for clarity. *Top two*: observed count spectrum vs. model. *Top Left* shows the Band function fitting and *Top Right* shows the mBB model fitting. *Bottom two*: the de-convolved photon spectrum plots. *Bottom Left* shows the Band function fitting, red line is the theoretical photon spectrum of the Band function and data points are the “observed” photon flux which is obtained by de-convolving the observed count spectrum using instrument responses. *Bottom Right*: same as *Bottom Left* but for the mBB model fitting where the red line is the theoretical photon spectrum of multi-color blackbody (mBB) model.

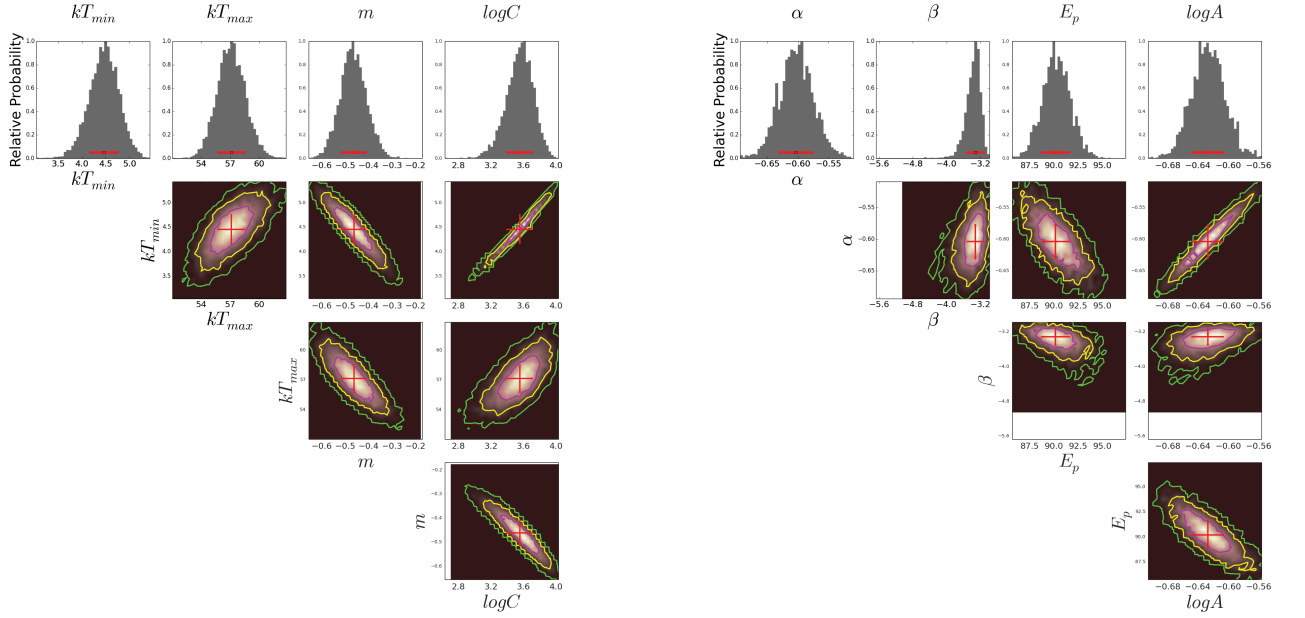


Fig. 6.— Parameter constraints of the mBB model (*left*) and Band function model (*right*) for time integrated spectrum between 20 and 30 s. Histograms and contours show the likelihood map of the parameter-constraint outputs by our *McSpecFit* package. Red crosses mark the best-fit values and 1-sigma error bars.

REFERENCES

- Abdo, A. A., Ackermann, M., Ajello, M., et al. 2009, *ApJ*, 706, L138
- Abramowicz, M. A., Novikov, I. D., & Paczynski, B. 1991, *ApJ*, 369, 175
- Atwood, W. B., Abdo, A. A., Ackermann, M., et al. 2009, *ApJ*, 697, 1071
- Axelsson, M., Baldini, L., Barbiellini, G., et al. 2012, *ApJ*, 757, L31
- Axelsson, M., & Borgonovo, L. 2015, *MNRAS*, 447, 3150
- Band, D., Matteson, J., Ford, L., et al. 1993, *ApJ*, 413, 281
- Basak, R., & Rao, A. R. 2013, *ApJ*, 768, 187
- Bégué, D., & Pe’er, A. 2015, *ApJ*, 802, 134
- Beloborodov, A. M. 2011, *ApJ*, 737, 68
- Borgonovo, L., & Ryde, F. 2001, *ApJ*, 548, 770
- Chandra, P., & Frail, D. A. 2008, *GRB Coordinates Network*, 8748, 1
- Cummings, J. R., Barthelmy, S. D., Baumgartner, W. H., et al. 2008, *GRB Coordinates Network*, 8708, 1
- Deng, W., & Zhang, B. 2014, *ApJ*, 785, 112
- Fan, Y.-Z., Wei, D.-M., Zhang, F.-W., & Zhang, B.-B. 2012, *ApJ*, 755, L6
- Gao, H., & Zhang, B. 2015, *ApJ*, 801, 103
- Ghirlanda, G., Pescalli, A., & Ghisellini, G. 2013, *MNRAS*, 432, 3237
- Goldstein, A., Burgess, J. M., Preece, R. D., et al. 2012, *ApJS*, 199, 19
- Golenetskii, S., Aptekar, R., Mazets, E., et al. 2008, *GRB Coordinates Network*, 8694, 1
- Golenetskii, S. V., Mazets, E. P., Aptekar, R. L., & Ilinskii, V. N. 1983, *Nature*, 306, 451
- Goodman, J. 1986, *ApJ*, 308, L47
- Gruber, D., Goldstein, A., Weller von Ahlefeld, V., et al. 2014, *ApJS*, 211, 12
- Guiriec, S., Connaughton, V., Briggs, M. S., et al. 2011, *ApJ*, 727, L33

- Guiriec, S., Daigne, F., Hascoët, R., et al. 2013, *ApJ*, 770, 32
- Hoversten, E. A., Baumgartner, W. H., Burrows, D. N., et al. 2008, *GRB Coordinates Network*, 8687, 1
- Ito, H., Nagataki, S., Ono, M., et al. 2013, *ApJ*, 777, 62
- Kaneko, Y., Preece, R. D., Briggs, M. S., et al. 2006, *ApJS*, 166, 298
- Kargatis, V. E., Liang, E. P., Hurley, K. C., et al. 1994, *ApJ*, 422, 260
- Kuin, N. P. M., & Hoversten, E. A. 2008, *GRB Coordinates Network*, 8703, 1
- Larsson, J., Racusin, J. L., & Burgess, J. M. 2015, *ApJ*, 800, L34
- Larsson, J., Ryde, F., Lundman, C., et al. 2011, *MNRAS*, 414, 2642
- Lu, R.-J., Hou, S.-J., & Liang, E.-W. 2010, *ApJ*, 720, 1146
- Lundman, C., Pe’er, A., & Ryde, F. 2013, *MNRAS*, 428, 2430
- Meegan, C., Lichti, G., Bhat, P. N., et al. 2009, *ApJ*, 702, 791
-
- Meng, Y.-Z., Geng, J.-J., Zhang, B.-B., et al. 2018, *ApJ*, 860, 72**
- Mészáros, P., & Rees, M. J. 2000, *ApJ*, 530, 292
- Mizuta, A., Nagataki, S., & Aoi, J. 2011, *ApJ*, 732, 26
- Pe’er, A. 2008, *ApJ*, 682, 463
- Pe’er, A., Barlow, H., O’Mahony, S., et al. 2015, *ApJ*, 813, 127
- Pe’er, A., & Ryde, F. 2011, *ApJ*, 732, 49
-
- Peng, F.-K., Liang, E.-W., Wang, X.-Y., et al. 2014, *ApJ*, 795, 155**
- Preece, R. D., Briggs, M. S., Mallozzi, R. S., et al. 1998, *ApJ*, 506, L23
- Rees, M. J., & Mészáros, P. 2005, *ApJ*, 628, 847
- Ryde, F. 2005, *ApJ*, 625, L95
- Ryde, F., Axelsson, M., Zhang, B. B., et al. 2010, *ApJ*, 709, L172

Ryde, F., & Pe’er, A. 2009, ApJ, 702, 1211

Salvaterra, R., Campana, S., Vergani, S. D., et al. 2012, ApJ, 749, 68

Schwarz, G. 1978, Annals of Statistics, 6, 461

Stroh, M. C., & Hoversten, E. A. 2008, GRB Coordinates Network, 8701, 1

Toma, K., Wu, X.-F., & Mészáros, P. 2011, MNRAS, 415, 1663

Uhm, Z. L., & Zhang, B. 2014, Nature Physics, 10, 351

Wei, J.-J., Wu, X.-F., & Melia, F. 2016, MNRAS, 463, 1144

Wilson-Hodge, C. A. 2008, GRB Coordinates Network, 8704, 1

Yu, H.-F., van Eerten, H. J., Greiner, J., et al. 2015, A&A, 583, A129

Zhang, B. 2011, Comptes Rendus Physique, 12, 206

Zhang, B.-B., Zhang, B., Liang, E.-W., et al. 2011, ApJ, 730, 141

Zhang, B.-B., Uhm, Z. L., Connaughton, V., et al. 2016, ApJ, 816, 72

Zhang, B.-B., Zhang, B., Castro-Tirado, A. J., et al. 2018, Nature Astronomy, 2, 69